Magnetic behavior of a laminated magnetic core in the presence of interlaminar faults: a simulation method based on fractional operators

B. Ducharne[1,2], H. Hamzehbahmani[3], R. V. Sabariego[4], Y. Gao[5]

[1] ELyTMaX IRL3757, CNRS, Univ. Lyon, INSA Lyon, Centrale Lyon, Université Claude Bernard Lyon 1, Tohoku University, Sendai, Japan.

[2] Univ Lyon, INSA-Lyon, LGEF EA682, F69621, France.

[3] Department of Engineering, Durham University, South Road, DH1 3LE, Durham, UK.

[4] KU Leuven, Dept. Electrical Engineering, Campus EnergyVille, 3600 Genk, Belgium.

[5] Faculty of Science and Technology, Oita University, Oita 870-1192, Japan.

Abstract

Stacks of grain-oriented silicon steel (GO FeSi) laminations play a crucial role as magnetic cores of power transformers. These cores undergo degradation over time due to corrosion, thermal cycles, etc. Geometrical abnormalities and residual stress from manufacturing processes exacerbate these degradation processes. Edge burrs can form around cut edges and lead to InterLaminar Faults (ILFs). In a recent work, we described an innovative method for simulating dynamical GO FeSi lamination hysteresis cycles. This method can be applied without any change to a stack of electrically isolated laminations, like in a magnetic core. It is especially easy when the working conditions impose a homogeneous behavior (B-imposed conditions). The simulation technique combines the resolution of the magnetic diffusion equation and a fractional differential equation as material law, yielding excellent simulation results across a broad frequency range with only two parameters accounting for the dynamic contribution. This new article outlines the successful extension of this simulation method to consider ILFs and predict their impact on the performances. For this, lamination stacks were initially simulated under full short-circuit conditions. Then, we used linear combinations between responses from these stacks and flawless ones. The simulation successfully reproduced the experimental data obtained for one or three aligned ILFs on several conditions. Then it was used to predict the behavior of additional aligned ILFs and/or different numbers of laminations in the simulated stack.

Keywords

Magnetic hysteresis, fractional derivatives, electrical steel, magnetic core, interlaminar faults

I – Introduction

The magnetic core in an electromagnetic energy converter is a fundamental component that serves essential purposes, including converting the electrical into mechanical energy (electrical motor) and vice versa (electrical generator). This conversion is indispensable for multiple applications, from powering industrial machines to generating electricity in power plants. The magnetic core helps to maintain a strong magnetic field within the converter and ensures its concentration and appropriate direction [1, 2].

A well-designed magnetic circuit can significantly improve the efficiency of an electromagnetic converter. The path for the magnetic flux should be optimized to minimize losses (hysteresis losses, eddy currents, etc.).

Most magnetic cores are made of electrical steel laminations (thin iron sheets coated with an insulating layer) for physical and financial reasons. Electrical steel is an iron-based alloy that may have from zero to 6.5 wt% silicon, but the usual content is about 3 wt% (higher concentrations result in brittleness during cold rolling) [3-5]. Electrical steel is tailored to approach optimal magnetic properties: high permeability, low coercivity, etc. Its grains can be oriented (GO FeSi, [5]) or not (NO FeSi, [4]), depending on the application and the distribution of the magnetic flux.

Condition monitoring of magnetic cores is critical to maintaining the reliability and performance of electromagnetic converters that rely on them [6]. Condition monitoring involves assessing the core health to detect abnormalities or potential issues in their early stage, preventing potentially catastrophic failures. The most common condition monitoring methods for magnetic cores include visual inspection, measurement of the core losses, and measurement of impedances and inductances [6].

Laminated magnetic cores can experience various sources of degradation over time, including the most detrimental: corrosion, thermal cycles, and vibrations [7-9]. Those degradation factors can be emphasized by geometrical abnormalities or residual stress coming from the manufacturing process. This process includes cutting, punching, stamping, and welding. All these manufacturing phases are potential sources of unexpected flaws. One of them, especially harmful, is called edge burr and is sometimes observable around the cut edges and punched holes [10, 12]. Edge burrs are sources of electrical contact with limited resistance between adjacent laminations, also known as InterLaminar Faults (ILFs). Edge burrs are not the only source of ILFs. Vibrations of loose windings and mechanical stress of different origins can also induce ILFs during operating time (see Fig. 1 for illustration). ILFs generate additional current loops in the magnetic cores, unexpected magnetic fields, and eddy currents between the shorted laminations [13]. The accumulation of these currents in a confined volume induces high local power loss, significant heat generation, and hot spots (see Fig. 1). A weak number of faults might have a limited impact on the overall electromagnetic converter performance. Indeed, it will probably not be detected using conventional quality assessment methods. Still, considering that some of these devices can be continuously used for more than 30 years, the cumulated values of these losses can reach a remarkable amount. Also, when ILFs are taking place on both sides of a lamination stack, as illustrated in Fig. 1 of [14], the amount of additional eddy currents is significant, and the consequence on the transformer efficiency cannot be neglected anymore.

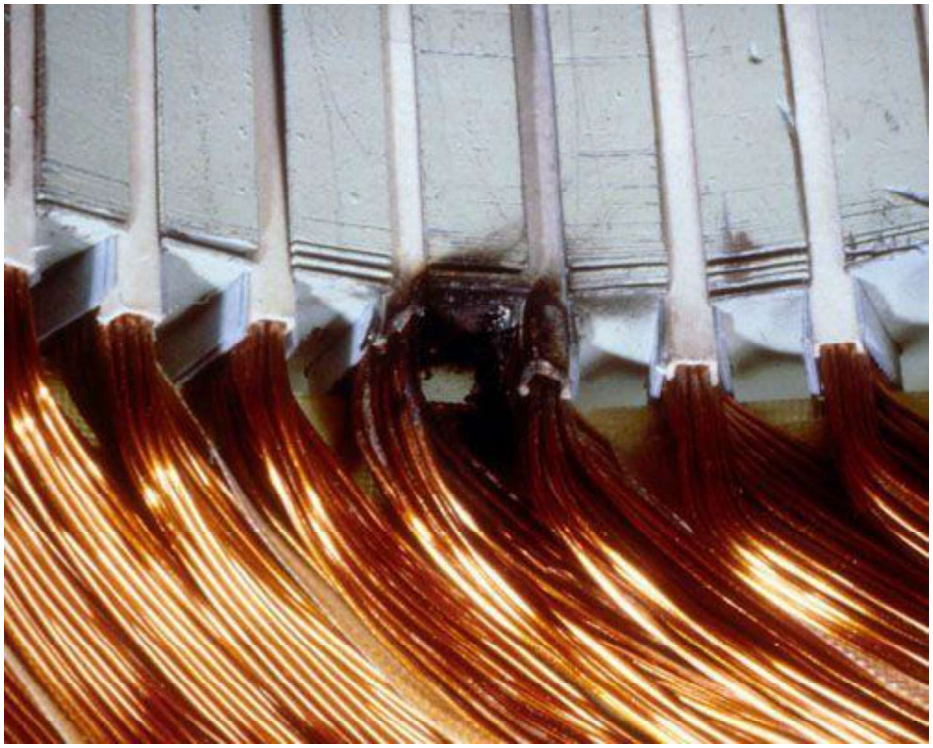

Fig. 1 – Core fault (ILF) in a three-phase induction motor due to arcing from the winding.

The need to address the issue of ILFs and the importance of a reliable condition-monitoring method for magnetic cores is now widely recognized by professionals in the field. It is accepted that the quality control of the magnetic core should be carried out proactively from the early stages to prevent ILF propagations and potential machine failure.

Magnetic laminated core quality assessment and condition monitoring are even emerging as active research topics, as illustrated by the recent prolific list of scientific papers [7-16]. Sophisticated experimental processes have been designed to precisely evaluate the impact of ILFs on the overall electromagnetic converter performances [17-19]. Some first tests of simulation methods have also been proposed, but they primarily focus on the power and thermal exchanges and leave the magnetic behavior of the laminated core unstudied.

In a recent paper [20], we have described an innovative simulation method of the magnetic behavior of a GO FeSi lamination. The simulation technique combines the resolution of the magnetic diffusion equation to a fractional order differential equation material law. Excellent simulation results have been obtained on a wide frequency range (up to more than 10 kHz [20]) with minimal parameters (only two parameters for the frequency-dependent contribution).

This new article describes how this simulation method has been extended successfully to consider ILFs and forecast their impact on magnetic core performances. After reviewing the fundamentals of the model and developing its extension, the numerical predictions are juxtaposed with experimental data for validation. The last sections comprise simulation predictions, discussions, and conclusions.

II – Simulation method

The simulation technique described in [20] and used in this study found its basis in the approach initially presented in [21]. This method simulates the magnetic behavior of a ferromagnetic lamination by simultaneously solving the magnetic field diffusion equation (Eq. 1) and a time-dependent material law. In a ferromagnetic lamination, the thickness ζ is very small vs. both the width and the length, and the resolution of the one-dimensional magnetic diffusion equation is enough to obtain accurate simulation results [22]:

$$\sigma \frac{\partial B(t,x)}{\partial t} = \frac{\partial^2 H(t,x)}{\partial x^2} \quad (1)$$

where, x is in the thickness ζ direction, σ is the electrical conductivity, B is the magnetic flux density, and H is the magnetic field strength. A finite-difference discretization is typically used for this resolution. The extensive frequency range tested in [23] showed that a first-order differential equation resolution (assimilated to viscous behavior, [21]) has limited accuracy and that much better results can be obtained with the fractional derivative term in Eq. 2. It reads:

$$\rho' \frac{d^n B(t)}{dt^n} = H(t) - H_{stat}(B(t)) \quad (2)$$

where, ρ' is a constant depending on the nature and the geometry of the tested specimen, n the fractional order, and $H_{stat}(B)$ denotes the magnetic excitation field H_{stat} required to obtain the magnetic flux density B in the quasi-static regime. In this study, to limit both discretization and memory management, such as saving simulation time, we opted for a static contribution $H_{stat}(B)$ obtained with the derivative static hysteresis model (DSHM), described in [24, 25]. This simulation method relies on a 2D interpolation matrix constructed with the columns and rows denoting the discrete values of H and B, whose terms represent the dB/dH slope at the corresponding point. As recalled in [24], DSHM can easily switch from H to B-imposed input conditions. To fill the DSHM matrix, experimental first-order reversal curves are promoted; however, obtaining such experimental data is always complex. In this work, we replaced them with simulated first-order reversal curves obtained with the J–A model [26, 27]. The J-A model was identified using the limited experimental data available (symmetrical quasi-static hysteresis cycles obtained for different levels of B). Additional details about the J-A and the DSHM models can be found elsewhere [24-27]. As described in [23][28, 29] and recalled hereafter for clarity, fractional derivatives are mathematical operators considering the frequency effect differently than an entire order derivative. It provides the simulation with an additional degree of freedom and accurate results on a significantly wider frequency range.

2.1 – Time-fractional derivative: physical meaning in a magnetic loss context and resolution

A time-fractional derivative extends traditional differentiation and integration calculus to include non-integer orders. Fractional derivatives are non-local by definition, i.e., where classical time derivatives can only describe changes next to current time t, fractional ones consider the whole simulated time interval. Therefore, time fractional derivatives are recommended for long-time heavy tail decays involving the entire history [30-32]. This property suits the ferromagnetic materials known to be heavily history-dependent.

A first-order differential equation appears well-suited for the simulation of ferromagnetic materials characterized by a homogeneous distribution of the domain wall motions and the associated microscopic eddy currents (limited diffusion effect like in a ferrite core [33]). The magnetic loss is fully dissipative in these conditions, and the domain wall motions behave as viscous elements. Unfortunately, in a GO FeSi lamination, the magnetic domain wall motions are viscous and elastic. Such viscoelastic behavior is obtained with the fractional derivative term in Eq. 2, where *n* is the fractional order that sets the ratio between the viscous and the elastic contributions. A similar behavior can be obtained in mechanics by considering a combination of elastic springs and dampers [34].

There is no single, universally agreed-upon definition of a fractional derivative because the concept of fractional derivatives is a complex and evolving area of mathematics with multiple interpretations and applications. The forward Grünwald-Letnikov definition adheres to the causality principle [23], so it was adopted in this study:

$$\begin{cases} D_f^n f(t) = \lim\limits_{h\to 0^+} h^{-n} \cdot \sum_{m=0}^{\infty} \frac{(-n)_m}{m!} \cdot f(t-mh) \\ (n)_m = \frac{\Gamma(n+m)}{\Gamma(n)} = m \cdot (m+1) \cdot \ldots (n+m-1) \\ (m)_0 = 1 \end{cases} \quad (3)$$

where $(n)_m$ is the Pochhammer symbol and Γ the gamma function.

2.2 – Simultaneous resolution of the diffusion equation and the fractional differential equation used as material law.

The simultaneous resolution of Eq. 1 and Eq. 2 is described in detail in [20]; the main ideas are summarized hereafter. It starts with the reformulation of Eq. 2 as proposed below and continues with the concatenation of Eq. 4 and Eq. 1, leading to Eq. 5:

$$\frac{\partial B}{\partial t} = \frac{d^{1-n}\left(\frac{H-H_{stat}(B)}{\rho\prime}\right)}{dt^{1-n}} \quad (4)$$

$$\frac{1}{\sigma}\frac{\partial^2 H}{\partial x^2} = \frac{d^{1-n}\left(\frac{H-H_{stat}(B)}{\rho\prime}\right)}{dt^{1-n}} \quad (5)$$

The left-hand side term of Eq. 5 is rewritten using finite differences, and the right-hand side with the forward Grünwald-Letnikov definition:

$$\frac{H(x-r,t)-2H(x,t)+H(x+r,t)}{r^2} = \sigma \cdot \lim_{h\to 0^+} h^{n-1} \cdot \sum_{m=0}^{\infty} \frac{(n-1)_m}{m!} \cdot \left(\frac{H(x,t-mh)-H_{stat}(B(x,t-mh))}{\rho\prime}\right) \quad (6)$$

Once the geometrical symmetries and the boundary conditions are set, a matrix system can be obtained for the entire simulation (Eq. 14 in [20]). The time-domain resolution involves solving this matrix system at each simulation step. It provides the local excitation field $H_i(t)$ and is followed by a local resolution of the material law, leading to the local $B_i(t)$. In the final stage, the cross-section flux density B_a is calculated by averaging the local induction, according to Eq. 7 (where *N* is the number of space discretizations):

$$B_a = \frac{\sum_{i=1}^{N} B_i}{N} \quad (7)$$

2.3 – Consideration of the interlaminar faults in the simulation method.

2.3.1 Lamination stacks fully short-circuited on the lateral sides

The ILFs in the simulation method have been considered through an incremental process. Instead of simulating directly local ILFs, starting with the situations illustrated in Fig. 2 is more straightforward. Here, stacks of two, three, and four laminations have been fully short-circuited on both lateral sides (in red) [14].

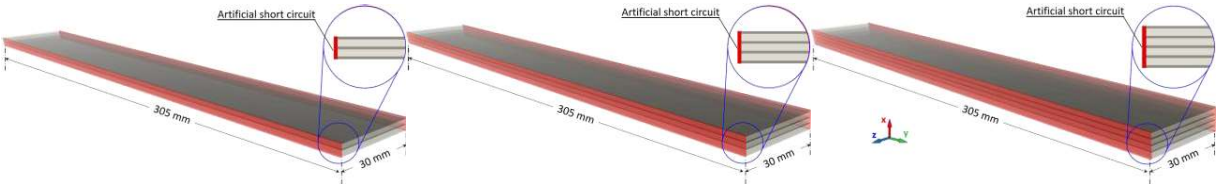

Fig. 2 – Stacks of two, three, and four laminations fully short-circuited on both sides along the length.

In a ferromagnetic lamination, a varying magnetic stimulus induces eddy currents. The eddy current distribution forms small loops through the cross-section and is ruled by a complex process involving multiple factors (frequency, geometrical, and physical properties). In conventional working conditions (f = 50/60 Hz), the amount of eddy currents is limited, with a relatively homogeneous distribution. In these conditions, the skin depth (Eq. 8) gives [0.4 – 1.5] mm for a typical GO FeSi (σ = 2.17 10^6 S m^{-1} and $\mu_r \in$ [1000 – 50000]), which is relatively large vs. the lamination thickness ζ.

$$\delta = \sqrt{\frac{2}{\omega\mu\sigma}} \quad \text{with} \quad \mu = \mu_0\mu_r \tag{8}$$

After assembling multiple laminations to form a stack and short-circuiting them on their lateral sides with a 500 µm thick layer of lead-free solder, a bulker component is created where additional eddy currents are authorized to circulate from one lamination to the others using the path offered by the low resistivity of the short circuits. The lead-free solder has an electrical conductivity of $\sigma_{lead\text{-}free\ solder}$ = 7.7 10^6 S·m^{-1}. The difference in the distribution of eddy currents is illustrated in the 2D finite elements simulation results depicted in Fig. 3. Stacks of two and four laminations are simulated with and without short circuits on their lateral sides. The eddy-current problem is modeled by the classical magnetic vector potential formulation [35-37]. Two distinct regions are visible: the first consists of the electrical steel laminations and the second includes the short circuit. We adopt a Jiles-Atherton vector hysteresis model for $H(B)$ (the hysteresis contribution) for the laminations and the vacuum permeability for the short circuits. Without short circuits, individual laminations in the stack show identical eddy-current distribution with a zero-net current (and net flux); all macroscopic eddy currents loop back in the lamination itself. With short-circuited stacks, individual laminations have a net current, and the stack exhibits an evident bulk behavior where the eddy currents loop through the short circuits on the lateral sides. This eddy current additional trajectory and the net current in the individual laminations cause further losses.

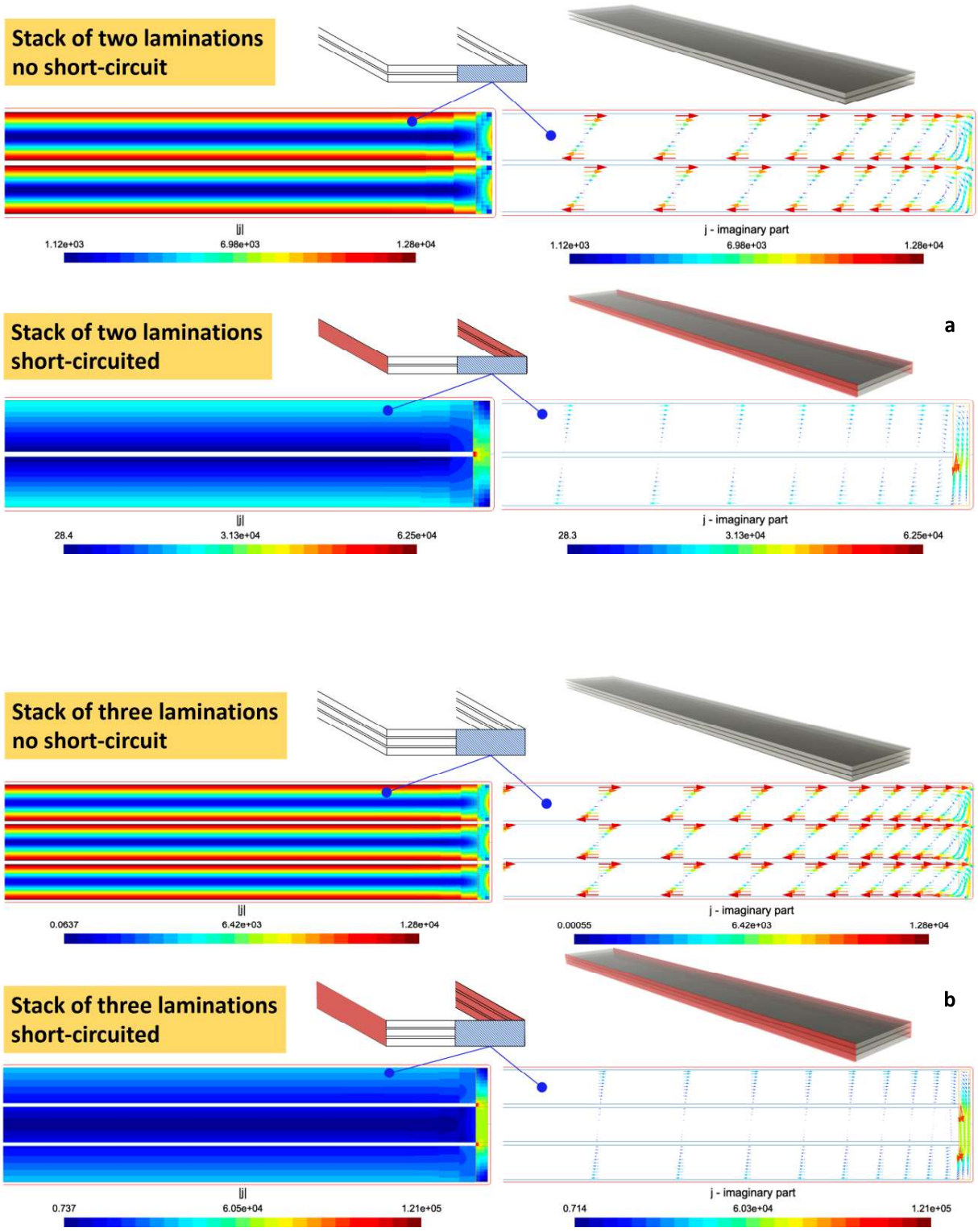
Stack of two laminations
no short-circuit
|j|
1.12e+03
6.98e+03
1.28e+04
j - imaginary part
1.12e+03
6.98e+03
1.28e+04
Stack of two laminations
short-circuited
a
|j|
28.4
3.13e+04
6.25e+04
j - imaginary part
28.3
3.13e+04
6.25e+04
Stack of three laminations
no short-circuit
|j|
0.0637
6.42e+03
1.28e+04
j - imaginary part
0.00055
6.42e+03
1.28e+04
Stack of three laminations
short-circuited
b
|j|
0.737
6.05e+04
1.21e+05
j - imaginary part
0.714
6.03e+04
1.21e+05

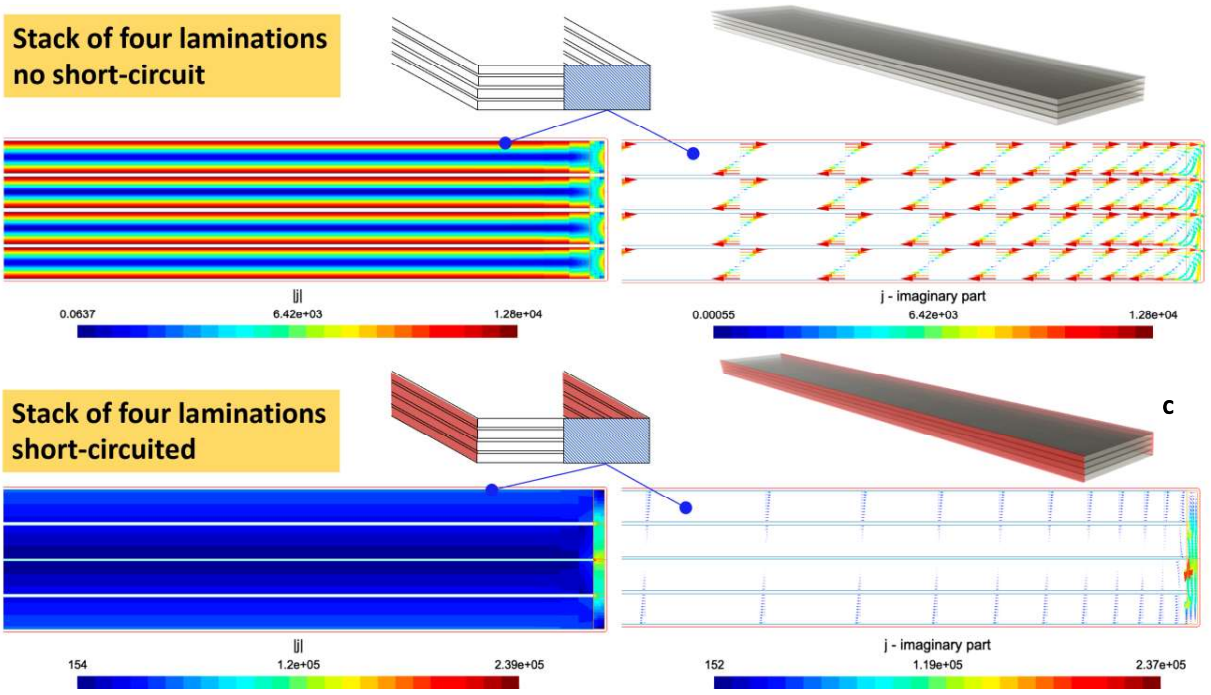

Fig. 3 – Eddy currents distribution obtained with finite element simulations through stacks of two (Fig. 3 – a), three (Fig. 3 – b) and four (Fig. 3 – c) laminations short-circuited or not on their lateral sides.

Of course, the short-circuited stacks do not behave precisely like bulk cores where the thickness ζ^* would equal the number of laminations times ζ. Still, similarities are high enough for the simulation previously described to be applied to the newly formed stacks with relatively good accuracies. Still, adjustments must be made to better match the experimental results, mostly by creating a degraded pseudo-conductivity σ^* ($S \cdot m^{-1}$) and using it as an equivalent σ. Table 1 below gives all the simulation parameters, and Fig. 4 depicts the evolution of σ^* as a function of the lamination number, with λ a constant.

Table 1 – Simulation parameters for the stack of laminations

	ζ^*	σ^*	n	ρ'
2 laminations	0.6 mm	$1.42\ 10^6$	0.98	0.0065
3 laminations	0.9 mm	$1.19\ 10^6$	0.98	0.0065
4 laminations	1.2 mm	$0.96\ 10^6$	0.98	0.0065

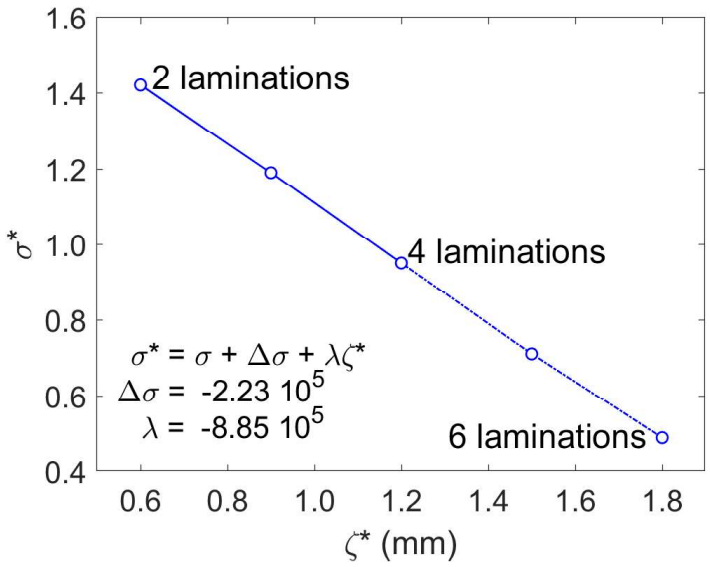

Fig. 4 – Pseudo conductivity σ^* as a function of the lamination stack thickness and the linear expression in terms of the conductivity σ, the stack thickness ζ^*, and fitted constants $\Delta\sigma$ and λ.

In this work, $\Delta\sigma$, λ, ρ', n and the quasi-static hysteresis parameters were obtained using the Euclidean difference criteria defined in Eq. 9 and based on fitting experimental measurements and numerical simulations. The quasi-static contribution (a combination of the Derivative Static Hysteresis Model [24, 25] and the Jiles-Atherton model [26, 27]) and the associated parameters were the same as in [20]. These parameters compiled in Table 2. ρ', n are given in Table 1, and $\Delta\sigma$, λ in Fig. 4.

$$\text{red}\ (\%) = 100 \cdot \sqrt{\frac{\int [meas(t) - sim(t)]^2 dt}{\int meas(t)^2 dt}} \tag{9}$$

Table 2 – Quasi-static contribution parameters

Quasi-static contribution parameters	Typical values
Ms	1.36 10^6 A·m^{-1}
a	1.5 A·m^{-1}
k	11.5 A·m^{-1}
c	0.06
α	7 10^{-6}

2.3.2 Lamination stacks partially short-circuited on the lateral sides (ILFs)

The second step of the simulation process consisted of considering local short circuits (aligned ILFs of 10 cm in length and short-circuiting the four laminations). Both cases (single and triple-aligned ILFs) illustrated in Fig. 5 have been studied.

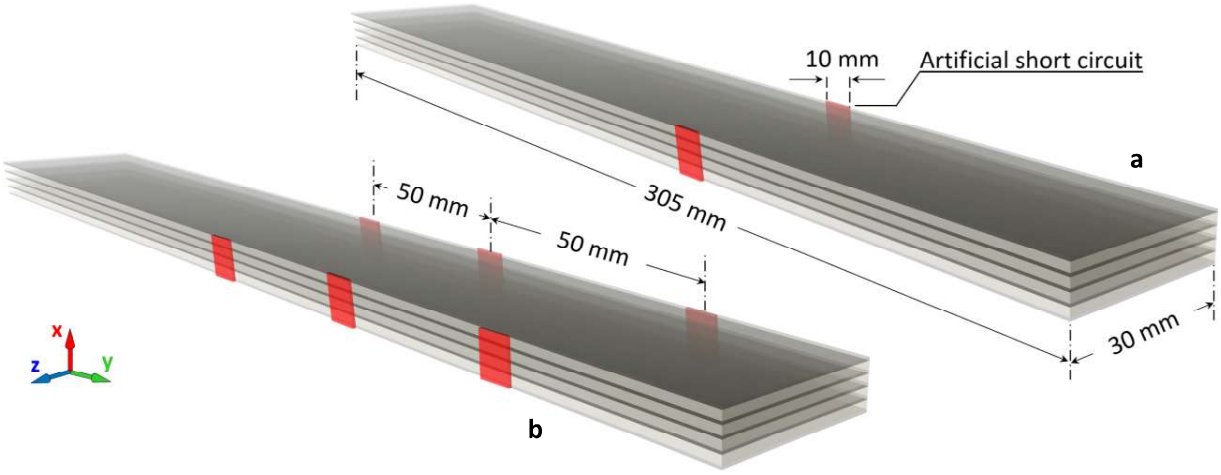

Fig. 5 – a Stack of laminations with one aligned ILF. **Fig. 5 – b** Stack of laminations with three aligned ILFs.

For this simulation, good results were obtained by combining the behavior of a flawless stack $H_F(B_a)$ and a fully short-circuited one $H_{SC}(B_a)$ similar to those of section 2.3.1. This combination relies on Eq. 10, 11 below obtained at a given flux density B_a:

$$H = \alpha H_F + \beta H_{SC} \quad (10)$$

$$\alpha + \beta = 1 \quad (11)$$

Assuming the number of aligned ILFs is small; this hypothesis always holds in the industrial context. In that case, α and β can be considered linearly dependent on it, and predictions can be obtained for the response of the lamination stack vs. different numbers of ILFs.

III – Description of the experimental results, comparison simulation/ measurement

3.1 – Experimental setup

In the experimental part of this work, standard Epstein-size strips of CGO 3 % SiFe, with a thickness of 0.3 mm and a measured electrical conductivity of $\sigma = 2.169\ 10^6\ S{\cdot}m^{-1}$, commercialized as M105-30P, were implemented. A computer-controlled magnetizing system based on a double yoke single strip tester (SST) was used to magnetize the test samples in line with the British standard BS EN 10280:2007 [38]. The tested electrical stack was positioned as illustrated in Fig. 7 of [37]. An $N_2 = 250$ turns secondary coil wrapped the tested stack, and an $N_1 = 865$ turns primary coil wrapped the secondary one. The voltage drop along the secondary coil was used to determine B_a, and the electrical current flowing through the primary coil was used for H_{surf}. All test samples were magnetized under controlled sinusoidal induction at peak flux densities of 1.0 T to 1.7 T and magnetizing frequencies of 50 Hz to 1 kHz. Uncertainty about this measuring system has already been validated according to the recommendations given in UKAS M3003 [39], which shows estimated type A and B uncertainties at ± 0.30 % and 0.63 %, respectively. Magnetic characteristics of the test samples, including dynamic hysteresis loop (DHL) and total power loss

in $W \cdot kg^{-1}$, have been measured and recorded separately for the range of magnetization. More details about the experimental setup are available in [37].

3.2 – Comparison simulation/measurement

3.2.1 – Comparison Simulation/Measurement for a single lamination and no ILF

The first series of results (comparisons simulation/measurement) shown in Fig. 6 has been picked up from [20]. These comparisons validate the simulation method in the case of a single lamination. The hysteresis and the excess loss are calculated using local static and dynamic hysteresis cycles; the classic losses are obtained through the iterative process described in [20]. The contributions and distributions of magnetic losses are depicted in the bottom part. Interested readers are referred to [20] for a detailed magnetic loss computational method description.

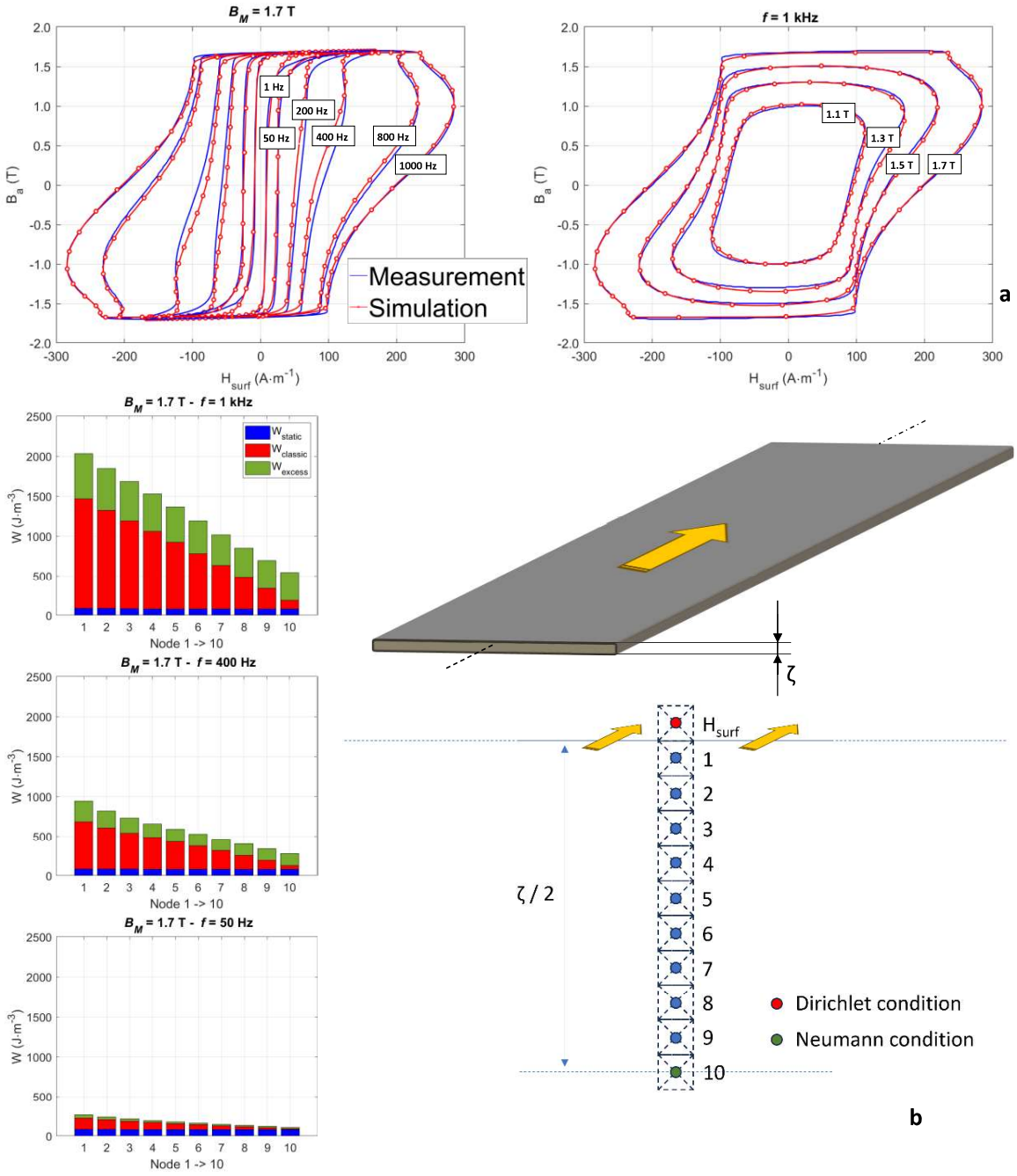

Fig. 6 – a Comparison simulation/measurement for a single lamination at different frequency and amplitude levels. **Fig. 6 – b** Distribution of the loss contributions.

Fig. 7 compares the magnetic behavior of a single lamination and a stack of four laminations without a short circuit. No significant difference is observed, which confirms that our simulation can be applied to the stack of laminations without any modification, including in the simulation parameters given in Table 1 and picked up from [20].

It is worth noting in Fig. 6 the invariance in the local distribution of the static loss contribution, which is primarily due to the shape of the static hysteresis behavior. This behavior shows almost

no induction variation once saturation is reached at a magnetic excitation level close to H_i = 100 A·m^{-1} (as illustrated in Fig. 4 of [20]).

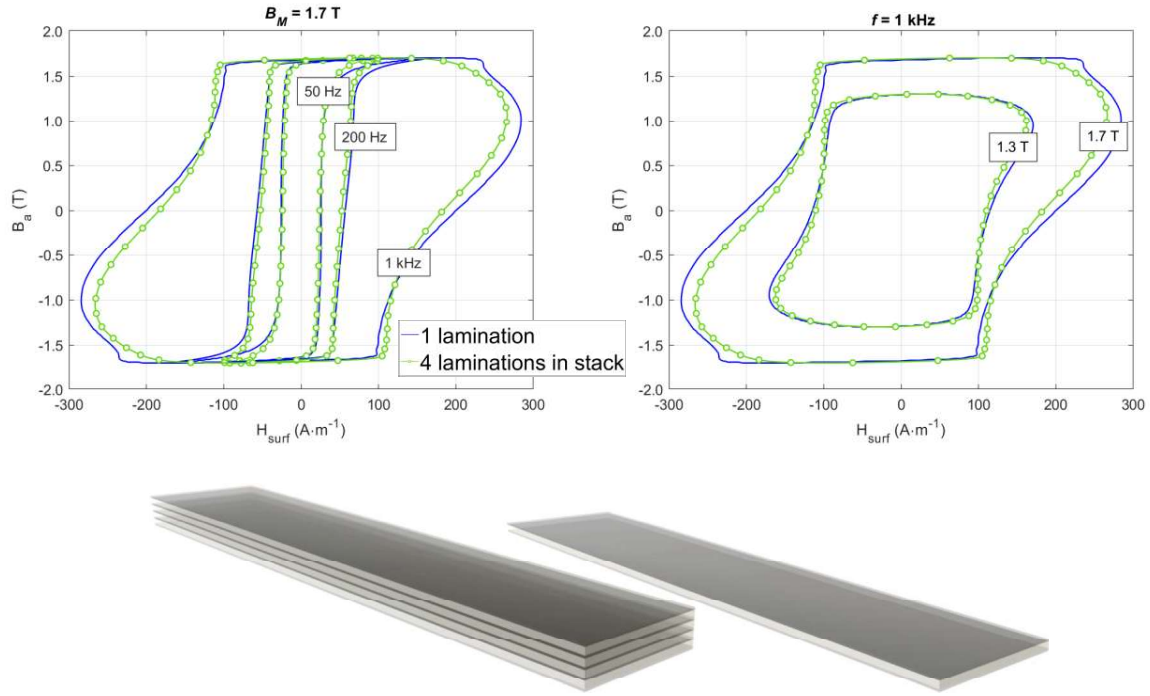

Fig. 7 – Comparisons between the GO FeSi experimental hysteresis cycles measured with a single lamination and a stack of four laminations.

3.2.3 – Comparison Simulation/Measurement for a single lamination and stack of two, three and four laminations fully short-circuited

The next comparison simulation/measurement series corresponds to the fully short-circuited lamination stacks. Stacks of 2, 3, and 4 laminations have been tested at B_M = 1.7T for f = 50, 200, and 1000 Hz and at B_M = 1.3T for f = 1000 Hz. Excellent simulation results have been obtained with the simulation parameters of Table 1, confirming the validity of the simulation method in this configuration. Better results can be seen in the higher frequency range, which probably denotes a limitation in the quasi-static contribution consideration.

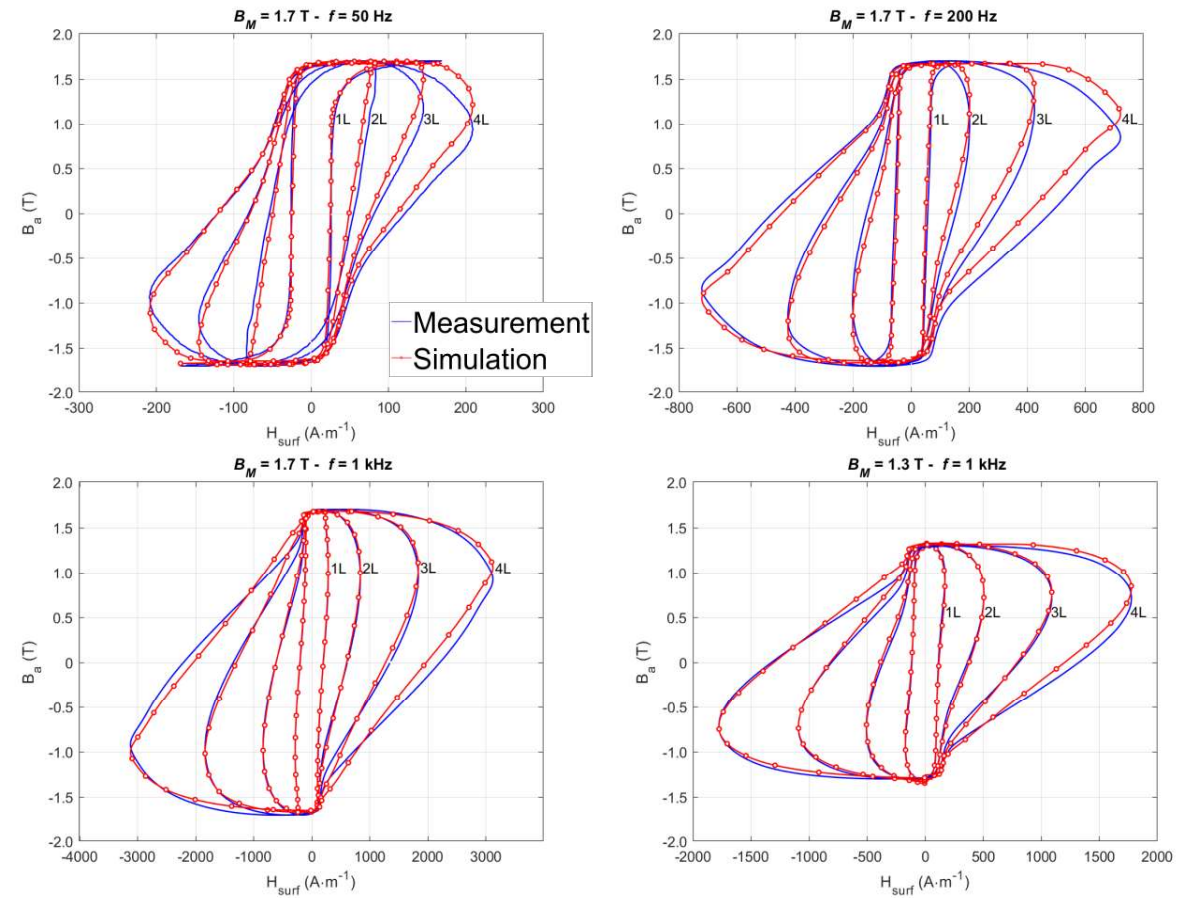

1L = 1 lamination

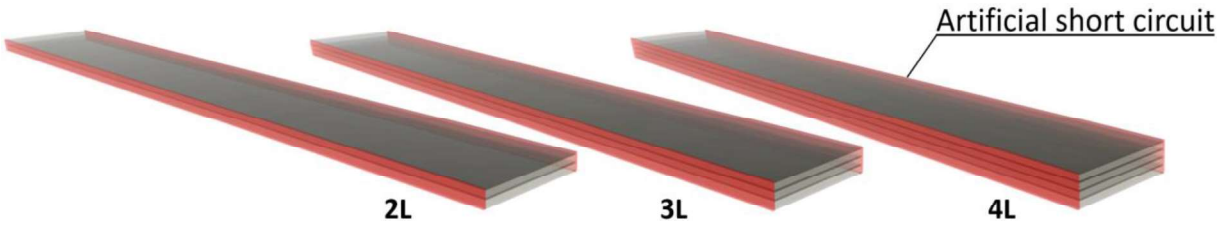

Fig. 8 – Comparison simulation/measurement for a single lamination, a stack of two, three, and four laminations fully short-circuited on their lateral sides at different frequency and amplitude levels ($\sigma = \sigma^*$, Table 1).

Fig. 9 illustrates the impact of σ by comparing the measurements and the simulations run with the excitation waveforms experimentally obtained at B_M = 1.7T and f = 1000 Hz but for $\sigma^* = \sigma$ = 2.17 10^6 S·m^{-1}. In this configuration, the higher conductivity of the resulting bulky specimen induces an intense eddy current distribution. The resulting shield limits the diffusion of the magnetic field to the upper part of the stack, and the average magnetic flux density falls drastically (simulated curve of the four laminations stack in Fig. 9).

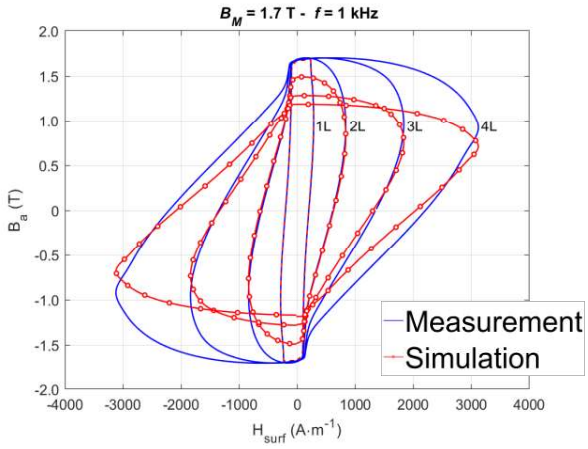

Fig. 9 – Comparison simulation/measurement for a single lamination, a stack of two, three, and four laminations fully short-circuited on their lateral sides at f = 1 kHz and B_M = 1.7 T (σ = 2.17 10^6 S·m^{-1}).

3.2.4 – Comparison Simulation/Measurement for a stack of four laminations locally short-circuited (one or three ILFs)

In this last series of comparisons Simulation/Measurement, a stack of four laminations has been successively locally short-circuited by one and three aligned ILFs (Fig. 5 – a and– b). 10 mm wide and approximately 500 µm thick ILFS were artificially introduced using lead-free solder. This material has a melting point far below that of electrical steel, and, more importantly, its conductivity is relatively close to that of electrical steel. Two values of B_M (1.3 and 1.7 T) and three frequency levels (50, 200, and 1000 Hz) have been tested. α and β were set again through the use of the Euclidean difference criteria (Eq. 8). The best values are given in Table 3:

Table 3 – Simulation parameters for one and three aligned ILFs consideration

number of aligned ILFs	α	β
1	0.885	0.115
3	0.76	0.24

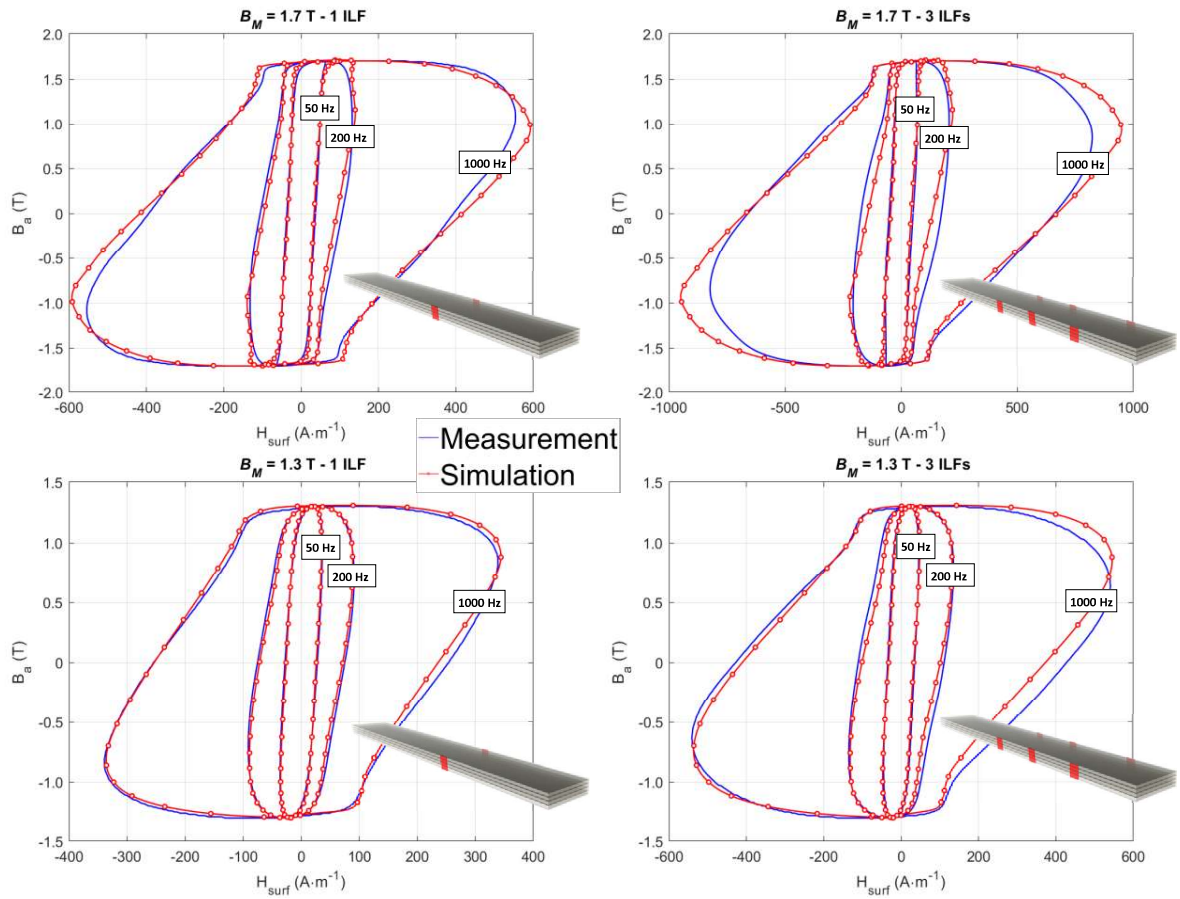

Fig. 10 – Comparisons simulation/measurement for a stack of four laminations and the presence of one or three ILFs (B_M = 1.3, 1.7 – f = 50, 200, 1000 Hz).

The excellent simulation results observed on the comparisons simulation/measurement depicted in Fig. 10 complete the validation of the method. In the next section, the predictive capability of the simulation method is exploited, including the magnetic core behavior in the case of two and four-aligned ILFs and the case of a higher number of laminations.

IV – Predictions and discussions

4.1 – Same number of laminations but additional ILFs

Estimating the additional energy loss due to aligned ILFs is straightforward. In [40], it was successfully demonstrated that this additional term does not influence the other loss contributions. It can be estimated by computing the difference in the hysteresis area of the lamination stack with and without defects [41]. Fig. 11 – a depicts the distribution of the losses vs. f in the case of Fig. 5 – a experimental situation, including one aligned ILF (readers are referred to [20] for a detailed description of the loss computation method).

Fig. 11 – b shows the influence of two to four aligned ILFs predicted with the simulation method. We have assumed a linear evolution of the additional loss term with the number of aligned ILFs.

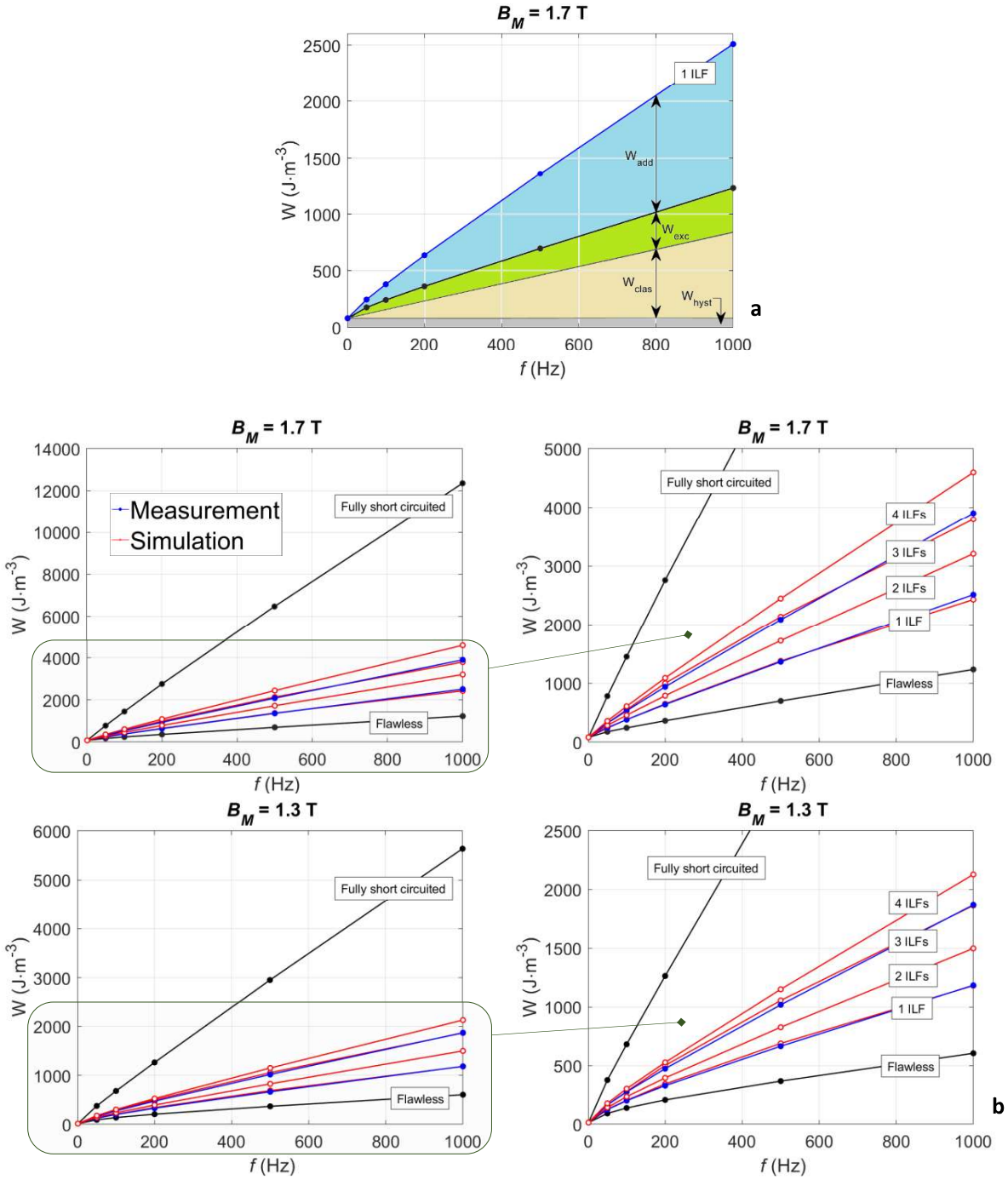

Fig. 11 – a Magnetic loss contributions, including the additional loss due to one aligned ILF. **Fig. 11 – b** Magnetic loss measured and predicted in the case of 1, 2, 3 and 4 ILFs.

The comparisons simulation/measurement of the loss variations in the presence of one and three ILFs depicted in Fig. 11 confirm the excellent accuracy of the simulation method. Regarding predictions, it is essential to note the limitations of the simulation method assumptions. These

limitations include assuming a linear evolution of the additional loss term, which only holds true when the number is small and each ILF is entirely independent.

4.2 – Same number of ILFs but different number of laminations

For the last series of predictions, the model was tested with a different number of laminations; we thus considered a 6-lamination. The fully short-circuited stack was simulated using the pseudo-conductivity displayed in Fig. 4 (σ^*= 490000 S·m^{-1}). As in [20], the Proportional-Iterative Learning Control (P-ILC) method described in [42] was used to return the B-imposed waveforms (Fig. 12 – a). Then, the impact of one and three aligned ILFs was simulated with parameters in Table 3. All results are depicted in Fig. 12 – b.

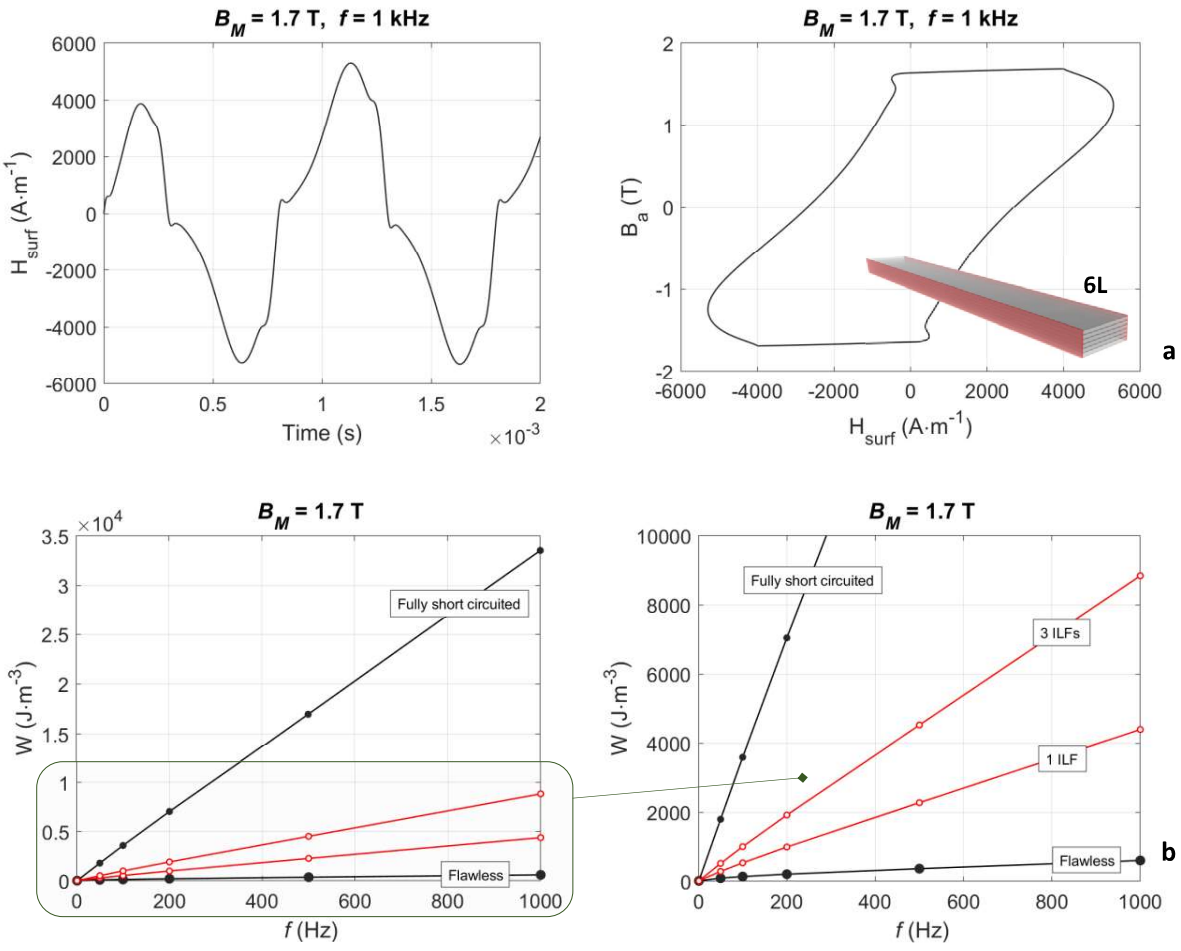

Fig. 12 – a Predicted time variations of the surface excitation field H_{surf} at B_M = 1.7 T and f = 1 kHz (left side) and the associated hysteresis cycle (right side) for a stack of six laminations fully short-circuited on their lateral sides.
Fig. 12 – b Magnetic loss predicted in the case of 1, and 3 ILFs in a stack of six laminations.

V – Conclusion

The simulation method described in this manuscript has been first developed to simulate the frequency-dependent hysteresis cycles of a GO FeSi electrical steel lamination. By simultaneously solving the Maxwell diffusion equation and a fractional differential equation material law, this method provides accurate simulation results on a broad frequency bandwidth with only two dynamical parameters (a constant ρ' and n the fractional order). The simulation method can be transposed to a stack of laminations in a B-imposed environment without modification. In these conditions, the behavior of each lamination is relatively homogeneous and can be easily transposed from the behavior of a single lamination.

In the first part of this work, stacks of laminations fully short-circuited on their lateral sides were simulated. In the model, these stacks are considered equivalent to a thick lamination characterized by a pseudo-conductivity. This equivalent behavior is evident in the finite element simulation results shown in Fig. 4. Stacks without short circuits show a similar pattern for each lamination (no net current). Oppositely, an explicit behavior at the stack scale (net current) can be observed for the short-circuited ones. The pseudo-conductivity characterizing the newly formed bulky element linearly depends on the number of constitutive laminations (Fig. 4). Excellent simulation results are obtained in this configuration.

Then, by combining the behavior of the short-circuited stacks with flawless ones, the measurements of a stack of four laminations, including one or three aligned inter-laminar faults, were accurately reproduced. Finally, the model's predictability was exploited by forecasting the variation of the magnetic loss in a stack of four laminations, including two and four aligned ILFs, and a stack of six laminations with one and three aligned ILFs.

This work constitutes a step forward in understanding ILF's influence on a magnetic core. The 1D resolution limits the number of space discretization and leads to very reasonable simulation times (less than 30s for a stack of four laminations). Future research will explore the impact of ILFs' alignment and how to consider it in the simulation methodology. The effect of the ILF length will also be examined, such as the distance separating two consecutive ILFs. Eventually, the nature of the short circuits (thickness, electrical conductivity) and the effect of symmetrical conditions will be assessed.

REFERENCES

[1] Hughes, A. and Drury, B., 2019. *Electric motors and drives: fundamentals, types and applications*. Newnes.

[2] Zacharias, P., 2022. *Magnetic Components: Basics and Applications*. Springer Nature.

[3] Moses, A.J., 1990. Electrical steels: past, present and future developments. *IEE Proceedings A (Physical Science, Measurement and Instrumentation, Management and Education)*, *137*(5), pp.233-245.

[4] Petrovic, D.S., 2010. Non-oriented electrical steel sheets. *Mater. Tehnol*, *44*(6), pp.317-325.

[5] Xia, Z., Kang, Y. and Wang, Q., 2008. Developments in the production of grain-oriented electrical steel. *Journal of Magnetism and Magnetic Materials*, *320*(23), pp.3229-3233.

[6] Kliman, G.B., Lee, S.B., Shah, M.R., Lusted, R.M. and Nair, N.K., 2004. A new method for synchronous generator core quality evaluation. *IEEE Transactions on Energy Conversion*, *19*(3), pp.576-582.

[7] Clerc, A.J. and Muetze, A., 2012. Measurement of stator core magnetic degradation during the manufacturing process. *IEEE transactions on industry applications*, *48*(4), pp.1344-1352.

[8] Kawaguchi, K., Takahashi, Y., Fujiwara, K., Matsushita, M., Takahashi, N. and Tokumasu, T., 2017. Basic investigation of deterioration on magnetic properties of laminated iron core after welding process. *International Journal of Applied Electromagnetics and Mechanics*, *55*(S1), pp.169-176.

[9] Helbling, H., Van Gorp, A., Benabou, A., Tounzi, A., Boughanmi, W. and Laloy, D., 2022. Analysis of magnetic properties degradation following industrial impregnation process of electrical steel laminations. *Journal of Magnetism and Magnetic Materials*, *563*, p.170008.

[10] Eldieb, A. and Anayi, F., 2016. Evaluation of loss generated by edge burrs in electrical steels. *IEEE Transactions on Magnetics*, *52*(5), pp.1-4.

[11] Hamzehbahmani, H., Anderson, P., Hall, J. and Fox, D., 2013. Eddy current loss estimation of edge burr-affected magnetic laminations based on equivalent electrical network—Part I: Fundamental concepts and FEM modeling. *IEEE transactions on power delivery*, *29*(2), pp.642-650.

[12] Hamzehbahmani, H., Anderson, P., Hall, J. and Fox, D., 2013. Eddy current loss estimation of edge burr-affected magnetic laminations based on equivalent electrical network—Part II: Analytical modeling and experimental results. *IEEE transactions on power delivery*, *29*(2), pp.651-659.

[13] Shah, S.B., Rasilo, P., Belahcen, A. and Arkkio, A., 2017, August. Experimental and theoretical study of interlaminar eddy current loss in laminated cores. In *2017 20th International Conference on Electrical Machines and Systems (ICEMS)* (pp. 1-6). IEEE.

[14] Hamzehbahmani, H., 2020. A phenomenological approach for condition monitoring of magnetic cores based on the hysteresis phenomenon. *IEEE Transactions on Instrumentation and Measurement*, *70*, pp.1-9.

[15] Fu, Q., Zhu, J., Mao, Z.H., Zhang, G. and Chen, T., 2017. Online condition monitoring of onboard traction transformer core based on core-loss calculation model. *IEEE Transactions on Industrial Electronics*, *65*(4), pp.3499-3508.

[16] Shin, S., Kim, J., Lee, S.B., Lim, C. and Wiedenbrug, E.J., 2015. Evaluation of the influence of rotor magnetic anisotropy on condition monitoring of two-pole induction motors. *IEEE Transactions on Industry Applications*, *51*(4), pp.2896-2904.

[17] Lee, S.B., Kliman, G.B., Shah, M.R., Kim, D., Mall, W.T., Nair, N.K. and Lusted, R.M., 2006. Experimental study of inter-laminar core fault detection techniques based on low flux core excitation. *IEEE Transactions on Energy Conversion*, *21*(1), pp.85-94.

[18] Romary, R., Jelassi, S. and Brudny, J.F., 2009. Stator-interlaminar-fault detection using an external-flux-density sensor. *IEEE Transactions on industrial electronics*, *57*(1), pp.237-243.

[19] Tallam, R.M., Lee, S.B., Stone, G.C., Kliman, G.B., Yoo, J., Habetler, T.G. and Harley, R.G., 2007. A survey of methods for detection of stator-related faults in induction machines. *IEEE Transactions on Industry Applications*, *43*(4), pp.920-933.
[20] Ducharne, B., Hamzehbahmani, H., Gao, Y., Fagan, P. and Sebald, G., 2024. High-Frequency Fractional Predictions and Spatial Distribution of the Magnetic Loss in a Grain-Oriented Magnetic Steel Lamination. *Fractal and Fractional*, *8*(3), p.176.
[21] Raulet, M.A., Ducharne, B., Masson, J.P. and Bayada, G., 2004. The magnetic field diffusion equation including dynamic hysteresis: a linear formulation of the problem. *IEEE transactions on magnetics*, *40*(2), pp.872-875.
[22] Zirka, S.E., Moroz, Y.I., Marketos, P. and Moses, A.J., 2006. Viscosity-based magnetodynamic model of soft magnetic materials. *IEEE transactions on magnetics*, *42*(9), pp.2121-2132.
[23] Ducharne, B. and Sebald, G., 2022. Fractional derivatives for the core losses prediction: State of the art and beyond. *Journal of Magnetism and Magnetic Materials*, p.169961.
[24] Scorretti, R., Sabariego, R.V., Sixdenier, F., Ducharne, B. and Raulet, M.A., 2011, July. Integration of a new hysteresis model in the Finite Elements method. In *Compumag 2011* (pp. n-334).
[25] Fagan, P., Ducharne, B. and Skarlatos, A., 2021, April. Optimized magnetic hysteresis management in numerical electromagnetic field simulations. In *2021 IEEE International Magnetic Conference (INTERMAG)* (pp. 1-5). IEEE.
[26] Jiles, D.C. and Atherton, D.L., 1986. Theory of ferromagnetic hysteresis. *Journal of magnetism and magnetic materials*, *61*(1-2), pp.48-60.
[27] Jiles, D., 2015. *Introduction to magnetism and magnetic materials*. CRC press.
[28] Ducharne, B., Zurek, S. and Sebald, G., 2022. A universal method based on fractional derivatives for modeling magnetic losses under alternating and rotational magnetization conditions. *Journal of Magnetism and Magnetic Materials*, *550*, p.169071.
[29] Ducharne, B. and Sebald, G., 2022. Combining a fractional diffusion equation and a fractional viscosity-based magneto dynamic model to simulate the ferromagnetic hysteresis losses. *AIP Advances*, *12*(3).
[30] Uchaikin, V.V., 2013. *Fractional derivatives for physicists and engineers* (Vol. 2). Berlin: Springer.
[31] Mainardi, F., 1997. *Fractional calculus: some basic problems in continuum and statistical mechanics* (pp. 291-348). Springer Vienna.
[32] Ducharne, B., Tsafack, P., Deffo, Y.A., Zhang, B. and Sebald, G., 2021. Fractional operators for the magnetic dynamic behavior of ferromagnetic specimens: An overview. *AIP advances*, *11*(3).
[33] Wilson, P.R., Ross, J.N. and Brown, A.D., 2004. Modeling frequency-dependent losses in ferrite cores. *IEEE Transactions on Magnetics*, *40*(3), pp.1537-1541.
[34] Meral, F.C., Royston, T.J. and Magin, R., 2010. Fractional calculus in viscoelasticity: an experimental study. *Communications in nonlinear science and numerical simulation*, *15*(4), pp.939-945.
[35] Gyselinck, J., Sabariego, R.V. and Dular, P., 2006. A nonlinear time-domain homogenization technique for laminated iron cores in three-dimensional finite-element models. *IEEE transactions on magnetics*, *42*(4), pp.763-766.
[36] Gyselinck, J., Dular, P., Krähenbühl, L. and Sabariego, R.V., 2015. Finite-element homogenization of laminated iron cores with inclusion of net circulating currents due to imperfect insulation. *IEEE Transactions on Magnetics*, *52*(3), pp.1-4.
[37] Hamzehbahmani, H., Sabariego, R.V. and Ducharne, B., 2024. A Knowledge-Based Analysis of Inter-Laminar Faults for Condition Monitoring of Magnetic Cores with Predominant Focus on Axial off-set Between the Fault Points. *IEEE Transactions on Instrumentation and Measurement*, Vol. 73, 3514710, pp. 1-10,
[38] BS EN 10280:2001 + A1:2007, Magnetic Materials-Methods of Measurement of the Magnetic Properties of Electrical Sheet and Strip by Means of a Single Sheet Tester (BSI, 2001).
[39] UKAS M3003, The expression of Uncertainty and Confidence in Measurement, Edition 4, Oct. 2019.

[40] Hamzehbahmani, H., Anderson, P. and Jenkins, K., 2015. Interlaminar insulation faults detection and quality assessment of magnetic cores using flux injection probe. *IEEE Transactions on Power Delivery*, *30*(5), pp.2205-2214.
[41] Hamzehbahmani, H., 2023. An Enhanced Analysis of Inter-Laminar Faults in Magnetic Cores With Grain Oriented Electrical Steels for Fault Diagnosis and Condition Monitoring: Theoretical Background and Experimental Verification. *IEEE Transactions on Instrumentation and Measurement*, *72*, pp.1-10.
[42] Fagan, P., Ducharne, B., Zurek, S., Domenjoud, M., Skarlatos, A., Daniel, L. and Reboud, C., 2022. Iterative methods for waveform control in magnetic measurement systems. *IEEE Transactions on Instrumentation and Measurement*, *71*, pp.1-13.